

X-ray reflection: a FLUKA model and its application in the design of synchrotron light beamlines and CERN’s Future Circular Collider

G. Mazzola,^{1, 2,*} S. Chitra,³ A. Devienne,¹ A. Frasca,^{1, 4} M. J. García-Fusté,⁵ D. Heinis,⁵ A. Lechner,¹ G. Lerner,¹ L. Rebuffi,³ M. Sanchez del Rio,⁶ D. L. Windt,⁷ E. Graugés,² and F. Salvat Pujol¹

¹*European Organization for Nuclear Research, Esplanade des Particules 1, 1211 Geneva 23, Switzerland*

²*Facultat de Física, Universitat de Barcelona, Martí i Franquès 1-11, 08028 Barcelona, Spain*

³*Argonne National Laboratory, 9700 S. Cass Avenue, 60439 Lemont, IL, USA*

⁴*University of Liverpool, Brownlow Hill, L69 7ZX Liverpool, UK*

⁵*ALBA Synchrotron, Carrer de la Llum 2-26, 08290 Cerdanyola del Vallès, Spain*

⁶*European Synchrotron Radiation Facility, 71 Avenue des Martyrs, 38043 Grenoble, France*

⁷*Reflective X-ray Optics LLC, 425 Riverside Dr., 10025 New York, USA*

Relying on atomic scattering factors from evaluated databases, a new model for the reflectivity of x rays on solid surfaces has been developed for FLUKA v4-6.0. This model accounts for the variation of reflectivity as a function of the photon energy, its incidence angle, and linear polarisation; surface roughness effects are also taken into account. FLUKA reflectivities agree well with those obtained from state-of-the-art codes used for the characterization of optical devices, both for homogeneous solids and for multilayer mirrors. This new capability renders FLUKA a nearly one-stop shop for synchrotron radiation simulations: emission from bending magnets and wigglers, photon transport and interaction, electromagnetic (and hadronic when applicable) shower development in complex geometries, as well as x-ray reflection at designated solid surfaces can now be all accounted for in a single FLUKA run. This streamlined FLUKA simulation workflow greatly simplifies the plethora of simulation tools that Monte Carlo practitioners previously needed to rely on. Two application scenarios of this new reflectivity model are showcased: first, the use of a multilayer mirror to deflect x rays from an optical hutch onto an experimental hall at the MINERVA beamline of the ALBA synchrotron and, second, the assessment of the photon flux near the interaction point at the CERN’s Future Circular Collider (in its electron-positron stage) as a result of upstream x-ray reflections.

I. Introduction

X-ray reflection is routinely exploited in synchrotron-radiation (SR) light sources for beam manipulation purposes: carefully positioned and oriented mirrors and multilayers are used to steer incoming x rays from an optical hutch towards experimental halls, and to perform wavelength filtering in the case of multilayers. Particle-transport simulations for such scenarios often involve a combination of tools [1–3]: a code for the generation of the SR source term [4–9], a general-purpose code for photon transport through the beamline and optical hutch [6–12] and, should x-ray reflection be considered, a further code for evaluating the x-ray reflectivity of the employed mirrors and multilayers [4, 5, 13, 14] before resuming the transport simulation in a further step. Alternatively, an ad-hoc analytical synchrotron radiation shielding code [4] can generate the SR spectrum from bending magnets or insertion devices and can also calculate the reflectivity for commonly used coated mirror. However, if detailed source terms or reflectivity from uncommon materials or complex configurations, as multilayer, are necessary, data from specialized codes [5, 13, 14] will need to be extracted and manipulated offline to then carry out the desired particle-transport analysis [2, 3]. The need for this combination of tools renders simulation studies rather unpractical.

The reflection of x rays also plays a surprisingly relevant role in high-energy electron/positron colliders. For instance, at the time of CERN’s Large Electron-Positron collider (LEP) [15], a machine with up to 104.5 GeV per beam, it was realised that upstream x-ray reflections substantially contribute to the photon background in the experimental regions [16]. Therefore, this effect is worth assessing in view of the ongoing design of CERN’s Future Circular Collider in its electron-positron mode (FCC-ee) [17].

To facilitate the laborious simulation workflow outlined in the first paragraph, while also providing a tool to address the issue raised in the second, a dedicated model for x-ray reflection on solid surfaces has been developed and implemented in the general-purpose particle-transport code FLUKA [6–9]. This work is structured as follows. In Section II, atomic-scattering factors from various evaluated photon data libraries are discussed and, based on them, the model implemented in FLUKA for x-ray reflection is presented. Its dependence on incidence angle, photon energy, and polarisation is highlighted, both for coated and multilayer mirrors, with surface-roughness effects taken into account. In Section III, this new FLUKA model for x-ray reflection in transport is benchmarked and validated against standalone state-of-the-art codes for x-ray optics [5, 13, 14]. The practical use of this novel FLUKA capability is demonstrated in two facility-design scenarios. In Section IV, a FLUKA simulation of the MINERVA beamline [18] at the ALBA synchrotron is presented, involving a multilayer mirror

* Contact author: giuseppe.mazzola@cern.ch

to steer a flux of x rays incoming from an optical hutch toward an experimental chamber. In Section V, the contribution of x-ray reflection to the photon flux around the interaction point of the FCC-ee is assessed. Finally, a summary and conclusions are presented in Section VI.

II. FLUKA model for x-ray reflection

A. Optical model

In the context of a general-purpose Monte Carlo code like FLUKA, where materials are assumed to be homogeneous and isotropic, coherent effects such as x-ray diffraction in crystals are generally disregarded [19]. Under these assumptions, the index of refraction $n(\mathbf{q}, \omega)$ of the material encountered by an incoming x ray can be constructed as [20]

$$n(\mathbf{q}, \omega) = 1 - \frac{r_e \lambda^2}{2\pi} \sum_s \mathcal{N}_s f_s(\mathbf{q}, \omega), \quad (1)$$

where ω is the photon frequency, λ is its wavelength, r_e is the classical electron radius, \mathcal{N}_s is the number of atoms of species s per unit volume, and the sum runs over all atomic species present in the material composition. The (complex) atomic scattering factors $f_s(\mathbf{q}, \omega)$ describe the absorption of a photon of frequency ω by an individual atom of species s [20–22] and the subsequent emission with a wavevector transfer \mathbf{q} . S -matrix calculations [23] suggest that for photon energies strictly below the K absorption edge (tens of keV for atomic numbers $Z \gtrsim 30$, order of keV for $30 \gtrsim Z \gtrsim 10$, and tens or hundreds of eV for $Z \lesssim 10$ [24, 25]), the variation of the atomic scattering factor for small \mathbf{q} is mild. Thus, the angle-independent atomic-scattering-factor (AIASF) approximation is adopted in this work, wherein $f_s(\mathbf{q}, \omega)$ is taken at zero momentum transfer:

$$n(\omega) \approx 1 - \frac{r_e \lambda^2}{2\pi} \sum_s \mathcal{N}_s f_s(\omega). \quad (2)$$

Despite the limited interval of validity for this expression, we have used it over the entire photon energy range considered in this work (from 100 eV up to 10 MeV). As shown below, the higher the photon energy, the more grazing (*i.e.*, small) the angle with respect to the surface has to be for the photon to be reflected. Thus, the small-angle approximation implied by Eq. (2) is anyway duly respected for all photon reflection energies covered in this work.

AIASFs are complex quantities, available from state-of-the-art evaluated atomic databases. Care should be exercised, since different libraries encode this quantity in slightly different ways. We have adopted the evaluated data of Henke *et al.* [20] as of August 2023 [26], in which AIASFs are tabulated as (dropping the subscript s to alleviate the notation)

$$f(\omega) = f_1(\omega) + i f_2(\omega), \quad (3)$$

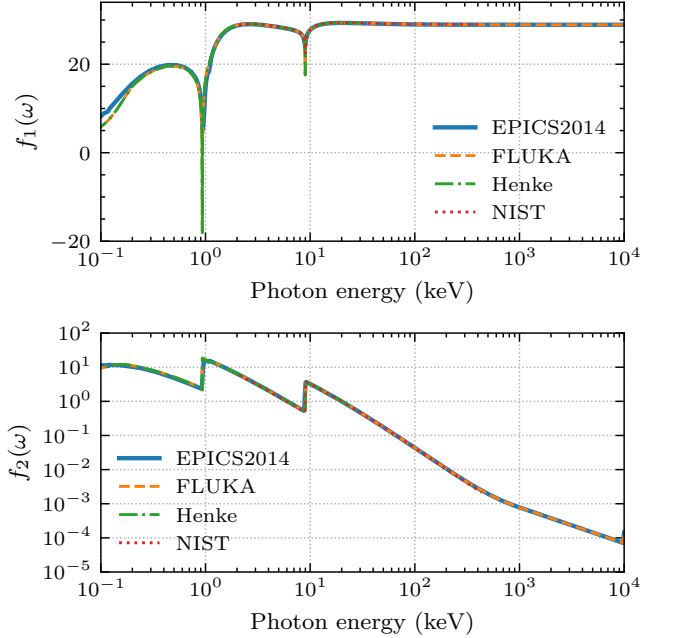


FIG. 1. Real (top) and imaginary (bottom) parts of the AIASF, Eq. (3), for Cu. Curves represent the values from EPICS2014 (solid), the extended Henke database employed in FLUKA (dashed), the original Henke data library (dash-dotted), and NIST (dotted).

where $\lim_{\omega \rightarrow \infty} f_1(\omega) = Z$ and $\lim_{\omega \rightarrow \infty} f_2(\omega) = 0$ [23]. This library covers photon energies from 50 eV up to 30 keV for atoms with $1 \leq Z \leq 92$. We have extended the Henke library to cover photon energies up to 10 MeV and atomic numbers up to $Z = 100$, such as to cover all material compositions allowed in the general-purpose Monte Carlo code FLUKA. This extension, henceforth referred to as extended Henke, has been performed relying on the EPICS2014 [25] database, wherein AIASFs are instead defined as

$$f(\omega) = Z + f'(\omega) + i f''(\omega), \quad (4)$$

where

$$f'(\omega) = f_1(\omega) - Z \quad (5)$$

is tabulated instead of the $f_1(\omega)$ term of the Henke database, while the adopted representation of the imaginary part remains unaltered: $f''(\omega) = f_2(\omega)$. A Kramers-Kronig analysis [20, 23] ensured the self-consistency of the obtained AIASF. Figure 1 displays the real (top) and imaginary (bottom) parts of the AIASF as a function of the photon energy for Cu, in anticipation of the application discussed in Section V. In this Figure, solid, dashed, dash-dotted and dotted curves represent EPICS2014, extended Henke (FLUKA), the original Henke library, and the NIST [27] library, respectively. Excellent agreement between EPICS2014 and Henke AIASF is observed in the range of photon energies

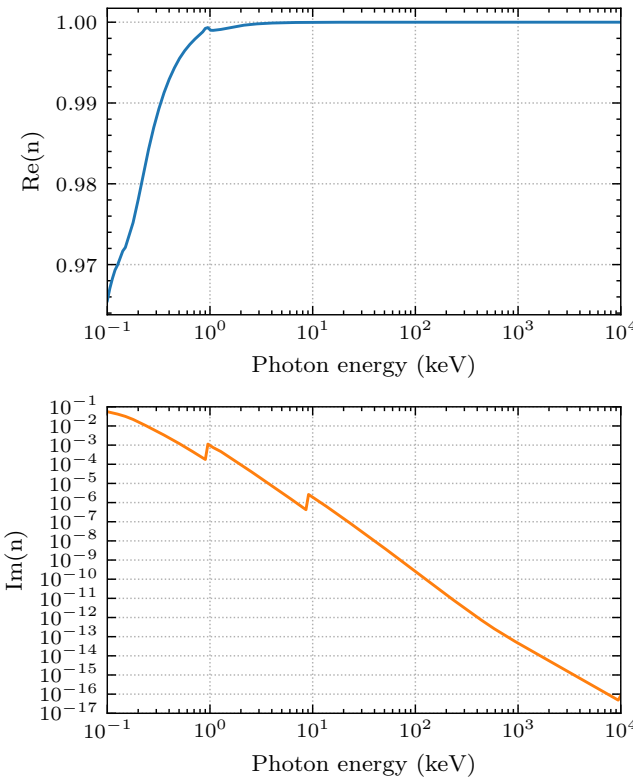


FIG. 2. Real (top) and imaginary (bottom) parts of the index of refraction of Cu, calculated with Eq (2) and the FLUKA extended Henke AIASF displayed in Fig. 1.

considered in FLUKA (above 100 eV), especially at energies above 1 keV, thereby justifying the extension of the Henke AIASF with those of EPICS2014 at high photon energies. The agreement extends also to the data from the NIST library covering the energy range from 2 keV to 433 keV. For later reference, Fig. 2 displays the real (top) and imaginary (bottom) parts of index of refraction of Cu, constructed with the prescription of Eq. (2) using the extended Henke AIASF displayed in Fig. 1.

The expression laid out above to construct indices of refraction, Eq. (2), applies for photon energies much higher than typical binding energies (order of eV or tens of eV). Thus, for photon energies approaching the FLUKA photon transport limit (100 eV) one might expect binding effects to start play a role, albeit minor. In this limit, experimental measurements or ab-initio calculations of $n(\omega)$ should be resorted to [28]. As further stressed below, a dedicated extension in the FLUKA implementation allows users to bypass Eq. (2) and load custom indices of refraction if needed.

B. X-ray reflectivity on the surface to homogeneous media

Photon reflection on solid surfaces at an outgoing angle matching the incoming one readily follows from

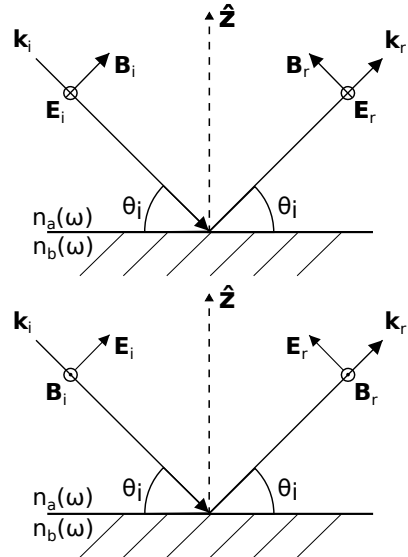


FIG. 3. Schematic layout of the wavevectors and electric field vectors employed in the evaluation of the reflection coefficient, Eqs. (6) and (7), for σ - (top) and π -polarised (bottom) x rays. Magnetic field components shown for completeness.

the boundary conditions of the Maxwell equations [20, 29, 30]. Figure 3 schematically displays a photon with wavevector \mathbf{k}_i propagating in a homogeneous medium a with index of refraction $n_a(\omega)$ and impinging on a homogeneous medium b , with index of refraction $n_b(\omega)$. The incoming photon wavevector forms an incidence angle θ_i with the planar surface. Both media are assumed to extend sufficiently far away from the boundary that one may disregard any potential reflection from the other end of the media. In the context of FLUKA, photon polarisation, albeit only linear, can be taken into account along a user-defined direction specifying the orientation of the electric-field vector \mathbf{E} , naturally normal to the photon wavevector. The top and bottom panels of Fig. 3 respectively display an incoming polarisation state \mathbf{E}_i normal (σ) and parallel (π) to the incidence plane spanned by the incoming wavevector \mathbf{k}_i and the surface normal $\hat{\mathbf{z}}$. This Figure also displays the wavevector \mathbf{k}_r of the reflected photon at an angle θ_i , along with a possible polarisation state. Magnetic field components \mathbf{B}_i are displayed for completeness. In such a scenario, the reflection coefficients for σ and π polarisation follow from the Fresnel equations [30], expressed here in terms of angles with

respect to the surface (and not the surface normal):

$$\begin{aligned} r_\sigma(\omega, \theta) &= \frac{E_{r\sigma}}{E_{i\sigma}} \\ &= \frac{n_a(\omega)\sin(\theta_i) - \sqrt{n_b^2(\omega) - n_a^2(\omega)\cos^2(\theta_i)}}{n_a(\omega)\sin(\theta_i) + \sqrt{n_b^2(\omega) - n_a^2(\omega)\cos^2(\theta_i)}}, \end{aligned} \quad (6)$$

$$\begin{aligned} r_\pi(\omega, \theta) &= \frac{E_{r\pi}}{E_{i\pi}} \\ &= \frac{n_b^2(\omega)\sin(\theta_i) - n_a(\omega)\sqrt{n_b^2(\omega) - n_a^2(\omega)\cos^2(\theta_i)}}{n_b^2(\omega)\sin(\theta_i) + n_a(\omega)\sqrt{n_b^2(\omega) - n_a^2(\omega)\cos^2(\theta_i)}}, \end{aligned} \quad (7)$$

that is as the ratio of reflected to incident electric field components for σ and π polarisation, respectively. From this definition, the reflected-photon electric field components follow readily:

$$\begin{aligned} E_{r\sigma} &= r_\sigma E_{i\sigma}, \\ E_{r\pi} &= r_\pi E_{i\pi}. \end{aligned} \quad (8)$$

Incidentally, the use of a complex index of refraction, as per Eq. (2), renders these expressions applicable for both dielectric and conducting media, and yields complex reflection coefficients. Thus, a phase shift between incident and reflected polarisation vector may easily be incurred. Figure 4 displays the phase shift for σ (top) and π (bottom) polarisation obtained as a function of photon energy for angles ranging from 1 to 100 mrad. The phase shift itself can even reach π at different photon energies depending on the incidence angle. This phase shift is disregarded here, since FLUKA currently tracks linear photon polarisation, defined by a unit vector with real (not complex) components. As shown below, the disregard of these phase shifts is often inconsequential for the likelihood of reflection: it is only problematic at very low photon energies (usually irrelevant in practical applications) and around the Brewster angle [30].

Not all photons impinging on a planar boundary reflect. The reflectivity (*i.e.* the likelihood of reflection) for σ and π polarisation (R_σ and R_π respectively) follows from the reflection coefficients [30]:

$$\begin{aligned} R_\sigma(\omega, \theta) &= |r_\sigma(\omega, \theta)|^2, \\ R_\pi(\omega, \theta) &= |r_\pi(\omega, \theta)|^2. \end{aligned} \quad (9)$$

Let P_σ and P_π be the σ and π polarisation-vector amplitudes for a photon with arbitrary linear polarisation, normalised such that $P_\sigma^2 + P_\pi^2 = 1$. Its reflectivity follows from Eq. (9):

$$R(\omega, \theta) = P_\sigma^2 R_\sigma(\omega, \theta) + P_\pi^2 R_\pi(\omega, \theta). \quad (10)$$

Finally, the reflectivity for an unpolarised photon beam reads

$$R(\omega, \theta) = \frac{R_\sigma(\omega, \theta) + R_\pi(\omega, \theta)}{2}. \quad (11)$$

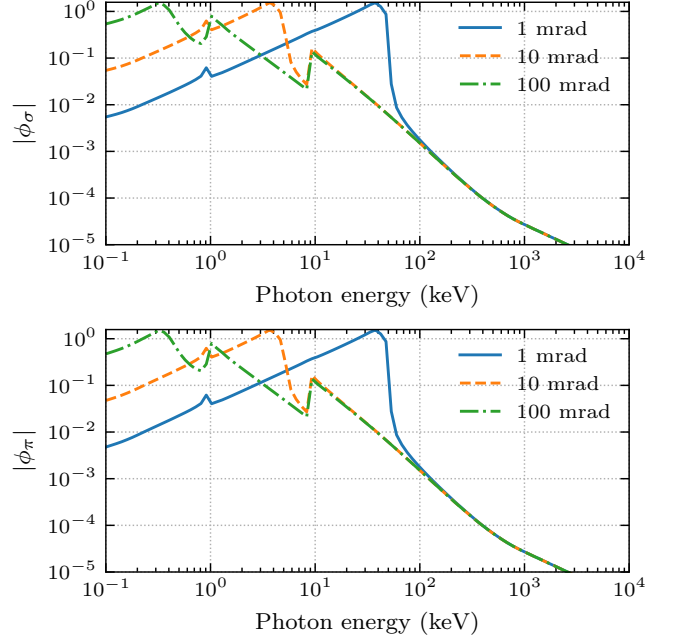


FIG. 4. Absolute value of the phase shift for σ - (top) and π -polarised (bottom) photons reflected from a homogeneous Cu slab as a function of the photon energy for 1 mrad (solid), 10 mrad (dashed), and 100 mrad (dot-dashed) incidence angle.

Figure 5 displays a bird's eye view of the σ (left) and π (right) reflectivity as a function of the photon energy and incidence angle, Eq. (9), for photons impinging from vacuum on Cu, computed using the index of refraction shown in Fig. 2. The reflectivities of both polarisation states are quite similar, except for a narrow band of angles near the Brewster angle (785 mrad) and photon energies below 1 keV in this example. To further elucidate this aspect, Fig. 6 displays the σ (solid curves) and π (dashed curves) reflectivities as a function of the photon energy for incidence angles of 10 mrad, 100 mrad, 785 mrad, and 1 rad. Indeed, accentuated discrepancies in reflectivity are found only near the Brewster angle at photon energies well below 1 keV. Thus, since σ and π reflectivities coincide in most of the energy and angular domain where the reflectivity is sizeable, the disregard of phase shifts between the σ and π components eluded to above is indeed inconsequential within the photon transport domain of FLUKA (energies above 100 eV). Note, however, that the model presented here will still yield accurate reflection coefficients as a function of linear photon polarisation (at least for the first - and often most relevant - reflection) for photon energies down to 100 eV.

C. X-ray reflectivity on multilayer mirrors

The model outlined above describes x-ray reflectivity on the surface of a homogeneous solid. It has been shown

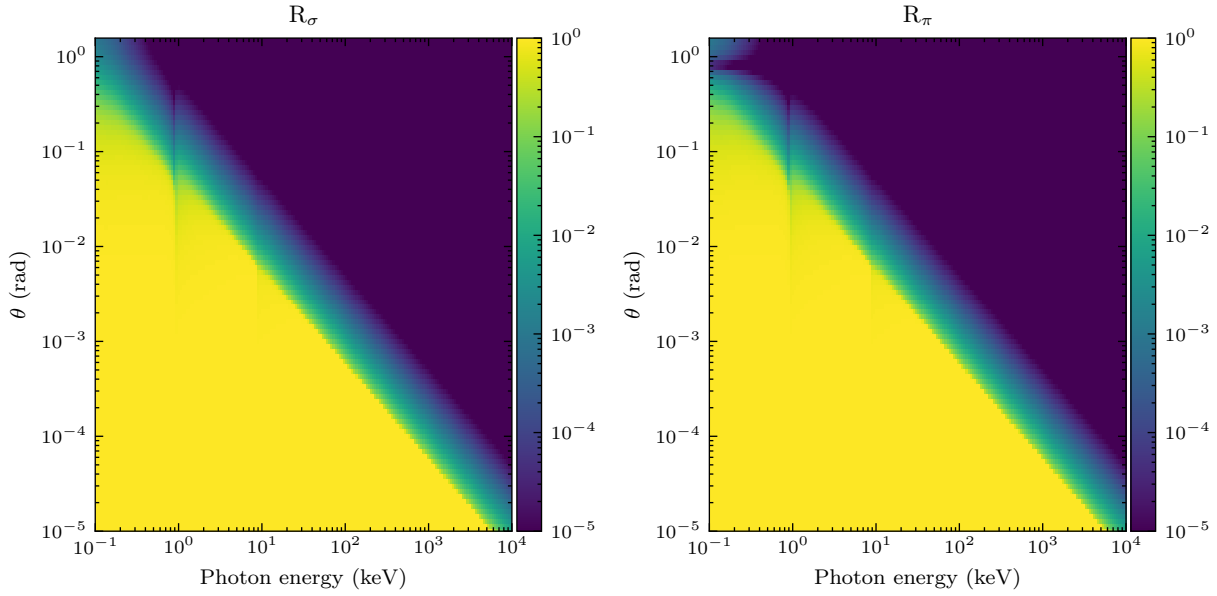


FIG. 5. Photon reflectivity of Cu as a function of energy and incidence angle for σ (left) and π (right) polarisation.

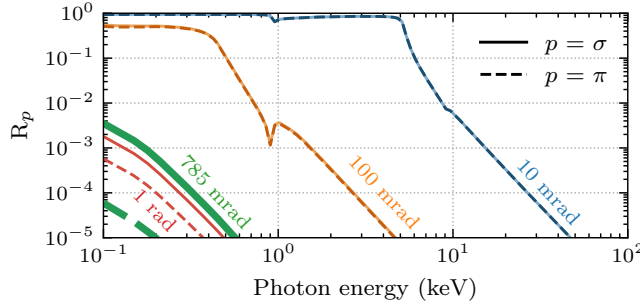


FIG. 6. Photon reflectivity of Cu as a function of energy for σ (solid) and π (dashed) polarisation, for selected angles near the Brewster angle (thick curves).

that reflectivity is highest for grazing angles and low photon energies. Multilayer mirrors (MLMs), instead, generally allow x rays to be reflected at larger angles and higher photon energies [31]. In addition, MLMs exhibit x-ray wavelength filtering capabilities and are therefore widely employed in optical beamlines of synchrotron-light sources to select a narrow range of photon wavelengths from the continuum SR spectrum generated by a bending electron beam. We have therefore extended our model to take into account x-ray reflectivity in MLMs.

The individual building block of a MLM is a group of two (or more) layers, typically alternating low- and high- Z materials, each with a well defined thickness, *e.g.* a Si layer of thickness d_1 and a W layer of thickness d_2 . The stacking of N_ℓ such groups of layers constitutes a MLM, typically limited by vacuum (or air) on one side and a substrate material on the other. Thus, the number of physical interfaces between different materials is (for two

layers in the individual building block) $2N_\ell + 1$, including the interface between vacuum/air and the first layer, as well as the interface between the last layer and the substrate.

Because of the periodic structure of a MLM, the reflectivity of an incident photon must account for the contribution of electromagnetic waves reflected on its various inner interfaces. Let $r_{p,2N_\ell+1}$ be the reflection coefficient of the interface between the last layer and the substrate, $r_{p,2N_\ell}$ that of the interface between the next-to-last and the last layer, and so on, for polarisation $p = \{\sigma, \pi\}$. The MLM is assumed to be thin enough that photon absorption within its volume is neglected and, furthermore, the substrate is assumed to be effectively a semi-infinite material, so that no photons are reflected back from its deeper regions, *i.e.*,

$$r_{p,2N_\ell+2} = 0 \quad (12)$$

for both polarisation states $p = \{\sigma, \pi\}$. This boundary condition allows us to evaluate the reflection coefficients of the subsequent upper layers of the MLM. Following Parratt [32], one may recursively evaluate

$$r_{p,j} = a_j^4 \frac{r_{p,j+1} + F_{p,j}}{1 + r_{p,j+1} F_{p,j}}, \quad (13)$$

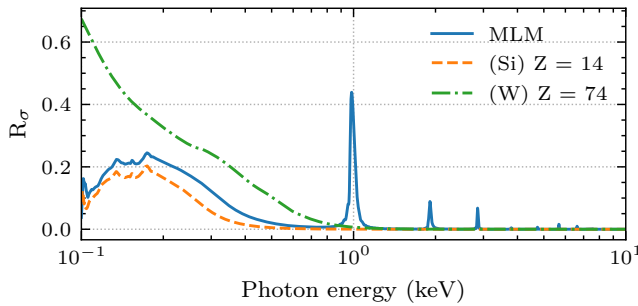


FIG. 7. Reflectivity for a σ -polarised photon, incident at 122 mrad on a multilayer mirror composed of Si-W layers (see text) on a Si substrate (solid line). Reflectivity of Si (dashed line) and W (dash-dotted line) shown for comparison.

for $j = 2N_\ell + 1, 2N_\ell, 2N_\ell - 1, \dots, 1$, where

$$F_{\sigma,j} = \frac{f_j - f_{j+1}}{f_j + f_{j+1}}, \quad (14)$$

$$F_{\pi,j} = \frac{\frac{f_j}{n_j^2} - \frac{f_{j+1}}{n_{j+1}^2}}{\frac{f_j}{n_j^2} + \frac{f_{j+1}}{n_{j+1}^2}}, \quad (15)$$

$$f_j = \sqrt{n_j^2 - \cos(\theta_i)^2}, \quad (16)$$

and $a_j = \exp(-i\pi f_j d_j \lambda^{-1})$ accounts for the phase shift accumulated by the photon as it traverses (half of) the layer j . All ω dependencies have been temporarily dropped to alleviate the notation. The reflection coefficients above allow us to directly set the polarisation state of the reflected photon. Instead, the reflectivity (*i.e.* the likelihood of reflection) of the MLM for σ and π polarisation is given by

$$R_\sigma = |r_{\sigma,1}|^2, \quad R_\pi = |r_{\pi,1}|^2. \quad (17)$$

For a photon with arbitrary linear polarisation, the reflectivity follows from a weighted sum of the reflectivities above, as in the case of reflection on the boundary to a homogeneous material, Eq. (10).

Figure 7 illustrates the reflectivity of a MLM consisting of 30 Si-W bilayers, with respective thicknesses of 4.1 nm and 1.2 nm, deposited on a Si substrate, for photon energies from 100 eV to 10 keV at an incidence angle of 122 mrad. The multilayer effects are visible with the appearance of a conspicuous maximum around 1 keV. Note that x-ray reflection on the boundary to a homogeneous material at these energies would not be possible for such a large incidence angle, as elucidated by the dashed and dot-dashed lines of the Figure, corresponding to the reflectivity on the surface to a homogeneous slab of Si and W, respectively.

D. Surface roughness

Finally, it should be noted that surface roughness greatly influences the reflection coefficient, both on homogeneous media and on MLMs. Due to this surface property, the normal vector is no longer constant: its orientation depends on the position on the surface. We do not expect to have a local map of the surface roughness; instead, we adopt the effective approach described by Nevot-Croce [33] and Sinha [34], as customary in x-ray software, whereby the reflection coefficient is attenuated by means of a factor

$$f_{NC} = \exp(-2k_{i\perp} k_{t\perp} R_q^2), \quad (18)$$

where $k_{i\perp}$ and $k_{t\perp}$ are the wavevector components normal (\perp) to the reflecting surface for both incident (i) and transmitted (t) photon, respectively, and R_q is the root-mean-square (RMS) average of the profile deviation from the mean height, as per ISO 4287 [35]. The RMS average usually depends on the manufacturing process of the specific component: it typically ranges from 25 nm to 50 μ m, although it can drop to values in the order of a few Ångström in x-ray mirrors. Since the wavevectors can be complex variables, the Nevot-Croce factor can itself be a complex quantity. This implies a change for both the amplitude and phase of the reflection coefficient. In the current FLUKA implementation, the phase shift induced by the roughness coefficient is disregarded for the same reasons invoked in the discussion of the reflectivity itself. Finally, we note that the Nevot-Croce factor is applied at every inner interface in the MLM reflectivity calculation.

III. Model validation

The x-ray reflectivity computed with the FLUKA model outlined above has been benchmarked against state-of-the-art codes for the characterization of optical devices, including XOP [5], XOPPY [13], and IMD [14]. These codes allow users the possibility of selecting different optical data libraries or even to provide their own. To assess the differences in reflectivity arising purely from the use of different codes, common optical data have been used among them, namely the Henke library, covering photon energies from 50 eV to 30 keV. Figure 8 displays the reflectivity of x rays impinging on a homogeneous slab of Cu (left) and Pt (right) as a function of their energy, from 100 eV (lower transport limit of photons in FLUKA) to 30 keV (upper energy limit of the Henke library), for incidence angles from 10^{-3} rad (top) to 10^{-1} rad (bottom), computed with FLUKA (solid curves), XOP [5] (dashed), XOPPY [13] (dot-dashed), and IMD [14] (dotted). Overall, very good agreement is observed among the four evaluations; the residual differences in the lower right-hand panel are due to the fact that FLUKA uses the latest version of the Henke library (as of August 2023) while the other codes rely on an earlier version.

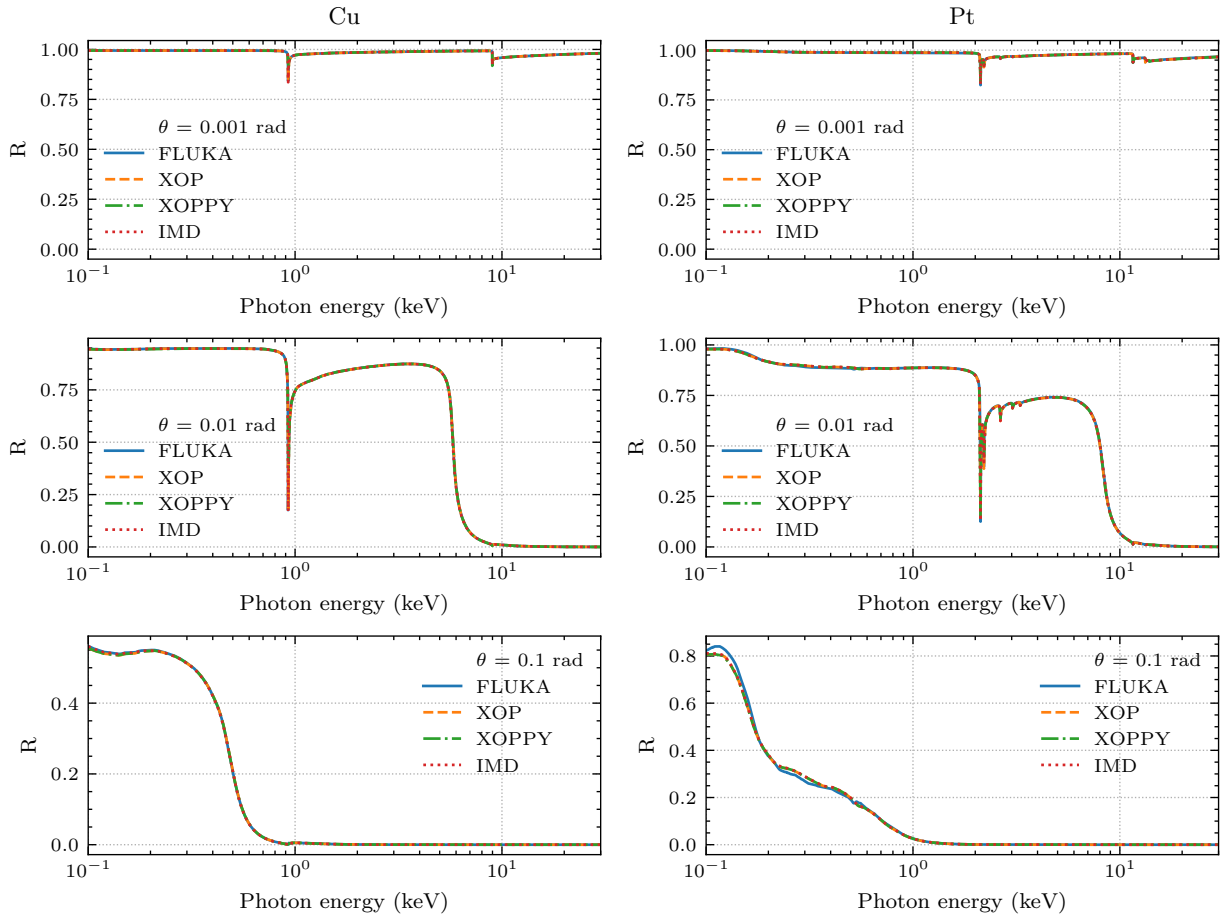


FIG. 8. Reflectivity of homogeneous Cu (left) and Pt (right) slabs as a function of photon energy, evaluated with FLUKA (solid curves), XOP (dashed curves), XOPPY (dot-dashed curves), and IMD (dotted curves) for unpolarised photons at the indicated incidence angles.

Similarly, Fig. 9 shows the x-ray reflectivity on the same photon energy scale and incidence angles for two MLMs: on the left for 30 Si-W bilayers (respectively 4.1 nm and 1.2 nm thick) on a Si substrate and, on the right, for 200 Mo-B₄C bilayers (respectively 2 nm and 4 nm thick) on a Si substrate. Note the absence of XOP curves for Mo-B₄C since the code does not support reflectivity calculations for MLMs with compound materials. The agreement among curves displayed in this Figure is also excellent, even in the region with a rich structure of peaks. Figure 10 extends the upper-left-hand panel of Fig. 9 to 433 keV showing curves calculated with FLUKA and IMD. While FLUKA still relies on the extended Henke data library, IMD curve is obtained employing NIST optical data [27] which covers the energy range from 2 keV up to 433 keV. Note the excellent agreement between the two curves also in this extended energy, in view of the fact that virtually identical optical data have been used strictly within the energy domain they cover.

While the FLUKA x-ray reflectivity model provided here is effective and generally applicable, two extension

capabilities are provided. On the one hand, the user routine `USRREF.f` allows users to input their own complex index of refraction, should they have experimental data or ab-initio calculations refining the incoherent addition performed in Eq. (1). On the other hand, the user routine `USRREF.f` allows users to adopt their own evaluation of the x-ray reflectivity, or to link to external tools such as XOP, XOPPY, and IMD.

IV. Application: the MINERVA beamline at the ALBA synchrotron

X-ray reflection at material interfaces is often exploited in the experimental beamlines of synchrotron light source accelerators. One or more mirrors are typically placed in the optical hutch of the beamline to filter and select a narrow interval of photon energies from the SR spectrum: when synchrotron radiation photons impinge on a MLM, the multilayer structure leads to reflection of photons within a narrow energy band. These are then transported to the experimental hutch in a stainless steel

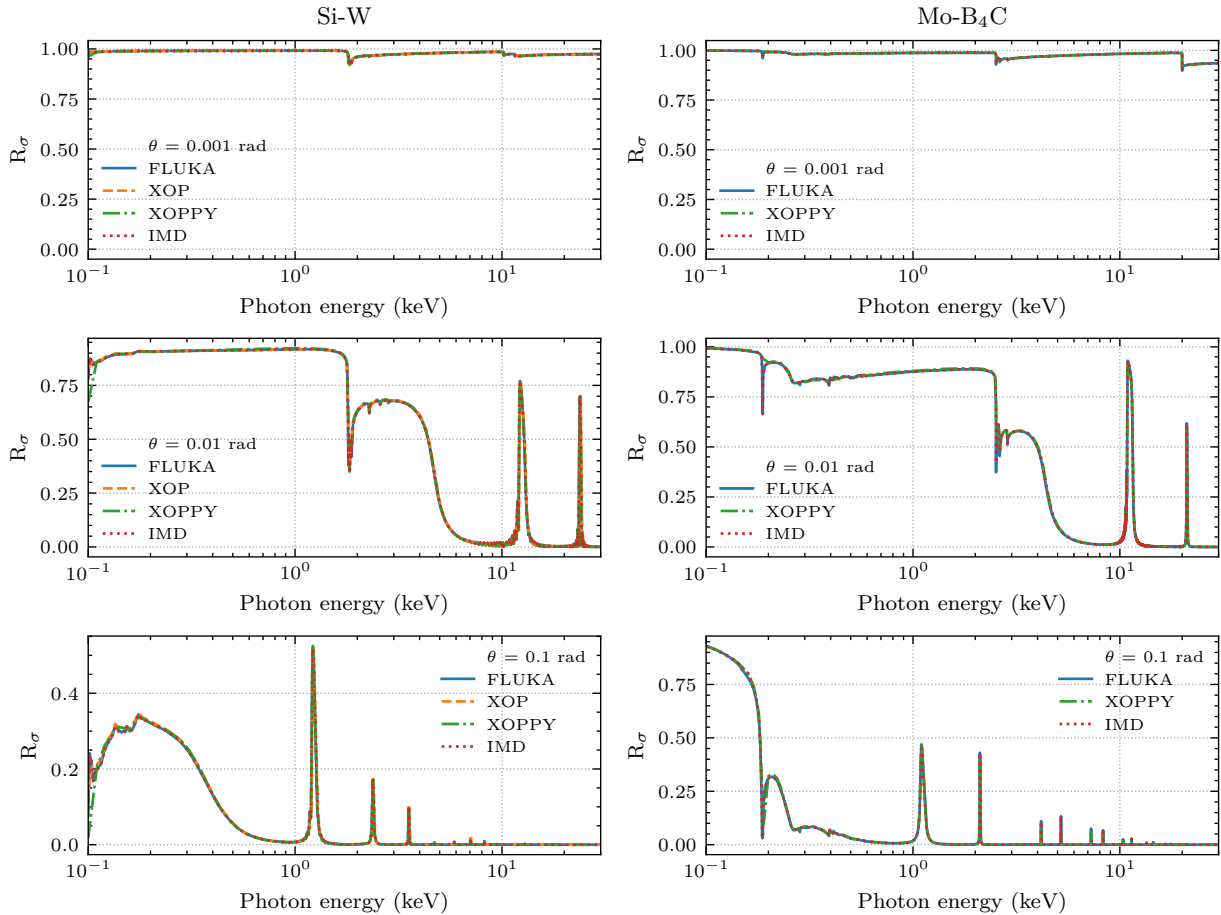


FIG. 9. Reflectivity as a function of photon energy for a Si-W (left column) and Mo-B₄C (right column) multilayer mirror (see text) evaluated with FLUKA (solid curves), XOP (dashed curves), XOPPY (dot-dashed curves), and IMD (dotted curves) for σ -polarised photons at the indicated incidence angles.

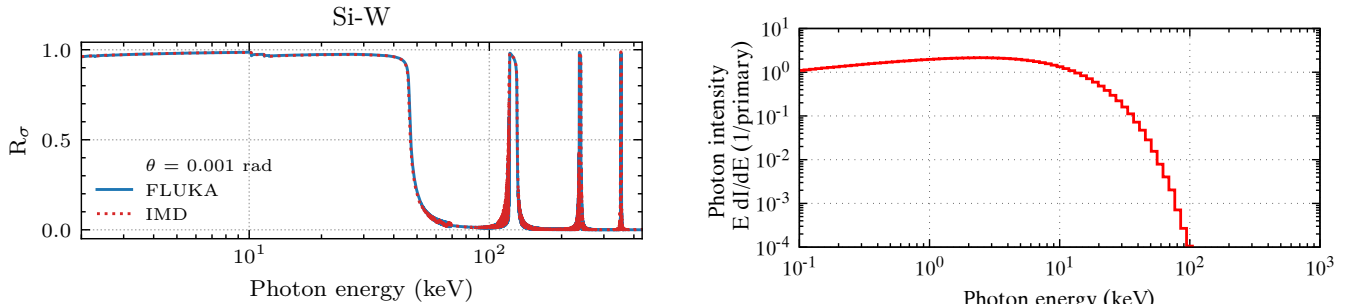


FIG. 10. Reflectivity as a function of photon energy for a Si-W multilayer mirror (see text) evaluated with FLUKA (solid curves) and IMD (dotted curves) for σ -polarised photons at the indicated incidence angle. The IMD calculation employs NIST optical data.

vacuum chamber, while any remaining part of the spectrum must be absorbed in appropriately placed shielding.

At present, various software tools are required to perform radiation studies for synchrotron light beamlines

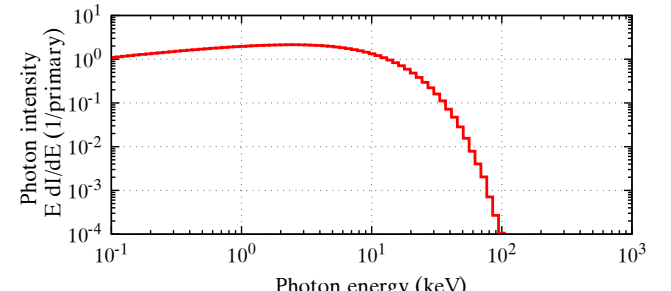


FIG. 11. Synchrotron radiation spectrum generated in FLUKA during the tracking along the full trajectory of a 3 GeV electron beam in a bending magnet of the ALBA storage ring.

involving x-ray reflection [1–3]: a code such as FLUKA, STAC8 [4] or XOP [5] for the generation of the SR spectrum from bending magnets and wigglers (in addition to undulators for the last two codes); a Monte Carlo code such as FLUKA for the transport along the beamline up

to the mirror; a further code for evaluating the x-ray reflectivity, such as XOP [5], XOPPY [13], or IMD [14]; a second-step Monte Carlo simulation to transport photons towards the experimental hall; and the necessary scripting to coordinate data transfer among tools.

To demonstrate FLUKA's integrated capabilities for the design of SR beamline facilities, a simplified geometry for the soft-x-ray MINERVA beamline at the ALBA synchrotron [18] has been implemented in FLUKA. The 3 GeV electron beam was used as source term (all simulation results below are given per primary electron). Electrons traverse a vacuum region of 1.384 m with a magnetic field of 1.42 T normal to the orbit plane, thereby acquiring a deflection of 11.25° [36]. While traversing this effective bending magnet, electrons radiate the SR spectrum displayed in Fig. 11. The emitted SR photons travel 16.66 m along the MINERVA beamline located in port 25 of ALBA storage ring with a restricted front end aperture of 0.48 mrad and, finally, reach the optical hutch of the experiment. There, the photons impinge upon a MLM (M1), consisting of 30 Si-W bilayers deposited on a Si substrate with thickness respectively of 4.1 nm and 1.2 nm, at a grazing angle of 7 deg, as shown in Fig. 12. The top panel of this Figure displays the photon fluence obtained with FLUKA v4-5.1, prior to the inclusion of the x-ray reflection model presented here. In absence of x-ray reflection, the SR photons impinging upon M1 are absorbed. The bottom panel of Fig. 12 displays the photon fluence obtained instead with FLUKA v4-6.0, equipped with the x-ray reflectivity model presented here: incoming SR photons impinging on M1 are clearly reflected towards the entrance of the experimental hutch. Naturally, not all photons are reflected, in accordance with the MLM reflectivity displayed in Fig. 7. The sharp peak at 1 keV in the multilayer reflectivity allows a flux of predominantly 1 keV photons to be reflected and transported further along the beamline. Note that in the geometry used for this simulation M1 is modelled considering the substrate material (Si) exclusively: the multilayer structure is 1 μ m thin, which is negligible as far as photon absorption and interactions are concerned.

A single FLUKA run sufficed to generate the SR spectrum from a bending magnet, to transport SR photon along the beamline, to handle the reflectivity on a multilayer mirror, and to further transport reflected photons to the experimental hutch. This integrated workflow considerably simplifies contemporary approaches relying on a concatenation of various tools [1–3]. Thus, FLUKA can be used as a single simulation tool to track SR photons from production to the optical beamline elements, thereby facilitating simulation studies, *e.g.* the analysis of thermal load on optical surfaces.

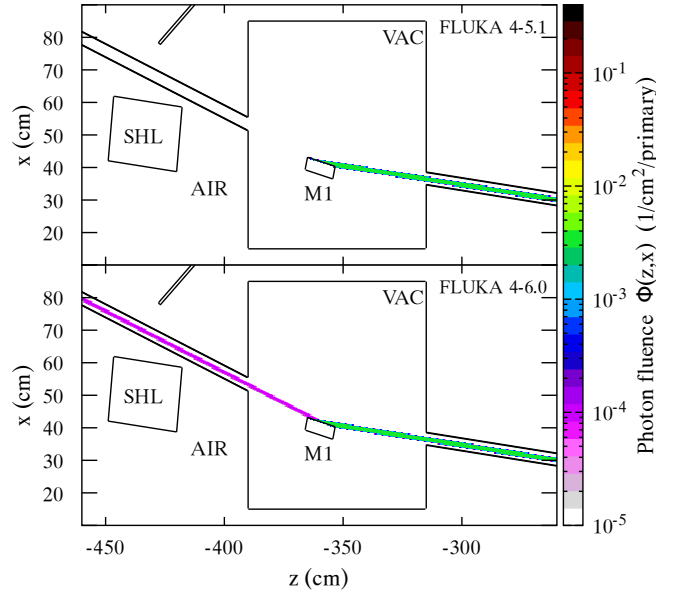


FIG. 12. Photon fluence in the optical hutch of MINERVA beamline at the ALBA synchrotron obtained with FLUKA 4-5.1 (top) and FLUKA 4-6.0 (bottom).

V. Application: the machine-detector interface for CERN's Future Circular Collider (FCC-ee) project

At the time of CERN's Large Electron-Positron (LEP) collider [15], it was already noticed that SR photons, particularly in the x-ray domain, can undergo reflection on the inner surface of the accelerator beam pipe, allowing them to reach downstream regions far beyond the first reflection point [16]. This phenomenon, in turn, can lead to a higher photon flux throughout the machine, an undesired background around the interaction point (IP), and radiation damage to the detector and the nearby beamline elements.

In view of the ongoing design of CERN's Future Circular Collider in its electron-positron (FCC-ee) configuration, it becomes relevant to assess the contribution of upstream x-ray reflections to the radiation background around the IP. To address this potential issue, the geometry of the machine-detector-interface (MDI) region of the FCC-ee was modelled in FLUKA [37], covering the last 720 m of the electron beam line towards the IP. This region includes magnetic elements as dipoles, quadrupoles, and sextupoles along the beamline, as well as a solenoid field in the detector area around the IP. In addition, collimators and SR masks are present. The FLUKA region corresponding to the inside of the beam pipe is assigned a vacuum material; inner-beam-pipe regions corresponding to the position of the aforementioned magnets have been assigned a magnetic field following version 24.4 of the Global Hybrid Correction (GHC) optical lattice [38–

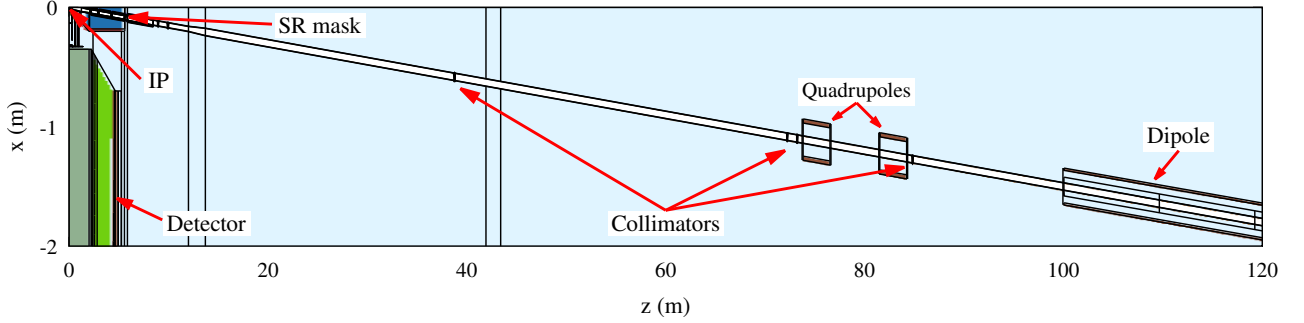


FIG. 13. FLUKA geometry model of the last 120 m of the FCC-ee MDI region.

40]. Figure 13 displays the adopted FLUKA geometry for the last 120 m of the FCC-ee electron line towards the IP.

Considering the Z-mode operation of the FCC-ee [41], a 45.6 GeV electron beam was used as source term in the simulations following the aforementioned optics. SR emission in transport [6] was enabled in FLUKA down to a threshold energy of 100 eV in all vacuum regions with magnetic fields. The solid curve in Fig. 14 shows the logarithmic spectrum of produced SR photons along the various magnets in the beamlne. Non-solid curves instead display the contributions from various magnetic field regions, namely from dipoles (dashed), from quadrupoles (dotted), and from the solenoid field around the IP (dash-dotted); sextupoles did not contribute appreciably. The dipole contribution, with its distinct critical energy (E_c) of 19.47 keV [30, 42] is dominant. However, a much higher-energy contribution due to SR emission in the solenoid field is also present, albeit of reduced relative importance.

The fluence of photons, differential in energy and in spatial coordinates was scored along the beamlne, including the region around the IP. Two FLUKA simulations were performed: on the one hand, a simulation with x-ray reflection switched off, representing the performances of FLUKA v4-5.1; on the other hand, a simulation with x-ray reflection activated at all interfaces between the beam-pipe vacuum and the materials of the beam pipe itself (Cu), as well as collimators (Mo-C alloy), and masks (W-Ni-Cu alloy), showcasing the enhanced capabilities of FLUKA v4-6.0.

Figure 15 displays the spatial fluence of photons in the last 20 m leading up to the IP, with photon reflection deactivated (top panel) and activated (bottom panel). A change of variables was performed to transform from the slanted beamlne of Fig. 13 (0.015 rad with respect to the z axis) to the arrangement of Fig. 15, wherein the beamlne is parallel to the u axis and perpendicular to the v axis. Indeed, in both panels the photon fluence increases in the last ~ 8 m to the IP in view of SR production in the final-focus quadrupole magnets and in the solenoid field around the IP, as discussed above. While the top panel (x-ray reflection off) exhibits a fairly monotonic photon

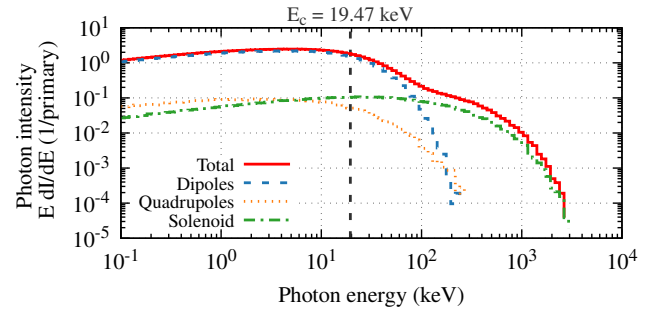


FIG. 14. FLUKA SR spectrum (solid curve) generated by the passage of a 45.6 GeV electron beam through the various magnets along the considered FCC-ee beamlne. The dashed, dotted, and dot-dashed curve represent the contribution from dipole, quadrupole, and solenoid magnetic fields. The vertical line indicates the critical energy (E_c) for SR emission in the dipoles.

fluence along the beamlne, the bottom panel (x-ray reflection on) shows that SR produced in the aforementioned magnetic field regions can indeed reflect multiple times along the beam pipe. This effect allows photons to reach downstream regions and, specifically, the region around the IP. Furthermore, discrepancies in photon spatial fluence due to x-ray reflectivity naturally accentuate at off-axis positions.

Figure 16 displays the energy-differential fluence of photons in a cylindrical region surrounding the IP, with a radius r of 1 cm and a length of 31 cm. This region is highlighted by a red box in Fig. 15. The solid curve in Fig. 16 was obtained with x-ray reflection switched off. Instead, the dashed and dotted curves were obtained with x-ray reflection activated, and an R_q parameter (see Eq. (18)) set to 25 nm and 0 nm respectively, the latter implying a perfect mirror surface. X-ray reflection at the beam pipe, collimators, and SR masks leads to an increase by a factor of up to 60% in photon fluence around the IP for perfect-mirror surfaces (dotted line). This enhancement naturally reduces with increasing surface roughness (see the dashed curve, where a sizeable effect is nevertheless still visible).

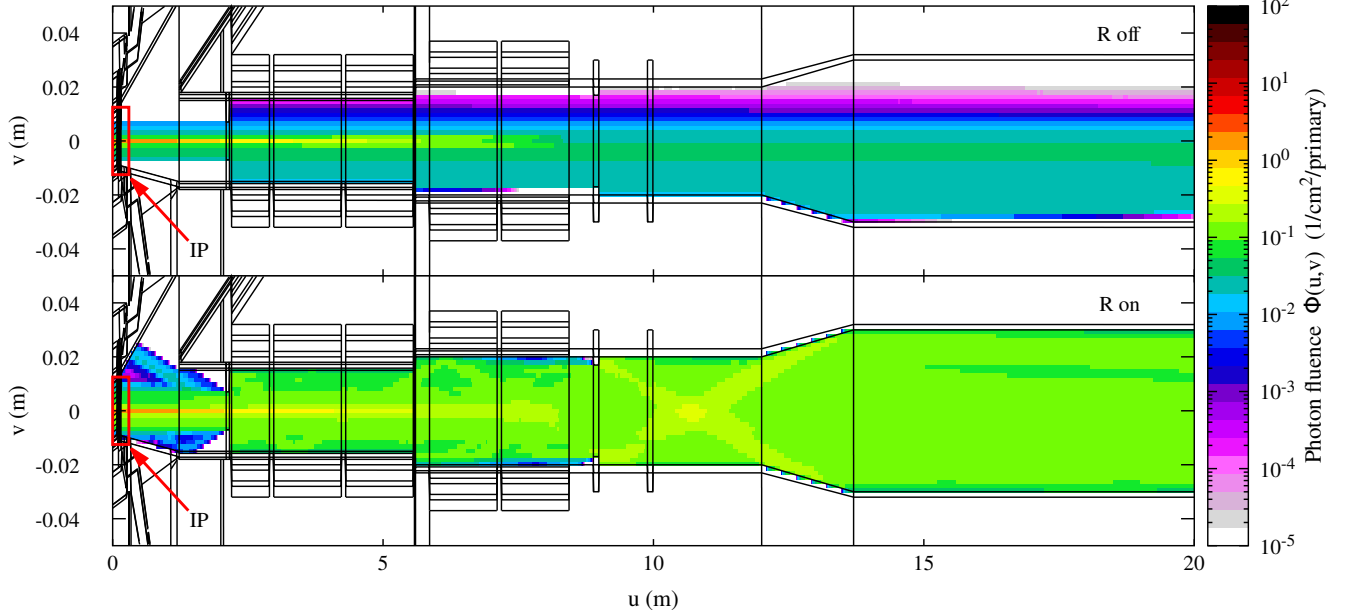


FIG. 15. Spatial photon fluence in the last 20 m of the MDI region of the FCC-ee in Z mode, obtained in FLUKA without (top) and with (bottom) x-ray reflection at the different vacuum-material interfaces (see text).

Figure 17 further resolves the energy-differential photon fluence in off-beam (radial) coordinate. The top panel restricts the cylindrical scoring volume around the IP to $r \in [0, 0.2]$ cm; the middle panel to $r \in [0.2, 0.4]$ cm (thicker lines) and $r \in [0.4, 0.6]$ cm (thinner lines); and the bottom panel to $r \in [0.6, 0.8]$ cm (thicker lines) and $r \in [0.8, 1.0]$ cm (thinner lines). Solid, dashed, and dotted lines carry the same meaning as in the foregoing Figure. As anticipated above, the largest discrepancies introduced by x-ray reflection are found at the farther off-beam radial regions. Still, in the closest region to the IP, x-ray reflectivity leads to differences in photon fluence of the order of 15%.

Thus, as was the case for LEP, x-ray reflection in upstream regions might indeed lead to a significant increase in the photon background in the detector region of the FCC-ee. The FLUKA x-ray reflection model presented in this work can therefore be readily employed to assess its magnitude in the design, *e.g.*, of bespoke SR masks and collimation systems for the FCC-ee.

VI. Summary and conclusions

Based on atomic scattering factors from evaluated photon data libraries, a new model for the reflection of x rays on solid surfaces and multilayer mirrors has been developed and implemented in FLUKA v4-6.0. The reflectivity is evaluated as a function of the photon energy, its incidence angle with respect to the surface, its (linear) polarisation state, and the roughness of the surface. Both

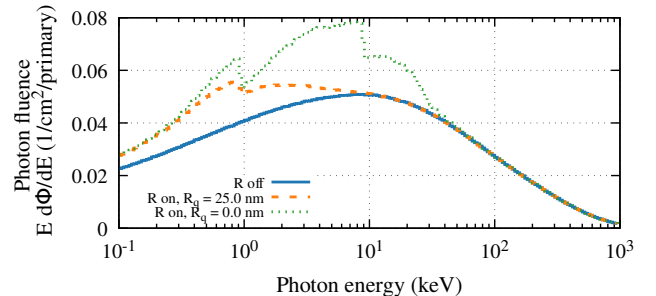


FIG. 16. Energy-differential photon fluence in a cylindrical volume around the Interaction Point (IP) of FCC-ee in Z mode (see text) with x-ray reflection deactivated (solid line) and activated on mirror-like surfaces (dotted line) and with a roughness characterised by $R_q = 25$ nm (dashed line).

homogeneous solids and multilayer mirrors are modelled. The reflectivity evaluated with this new model has been benchmarked against state-of-the-art codes for x-ray optics (XOP, XOPPY, IMD), obtaining very good agreement, both for mirrors and multilayers.

These enhanced capabilities allow a single FLUKA run to simulate the emission of synchrotron light by charged particles traversing bending magnets and wigglers (feature available since release 4-3.0 of FLUKA [6]), the transport of synchrotron radiation through complex geometries, the reflection on multilayer mirrors (or homogeneous solids such as the beam pipe itself), and the further transport of reflected photons. This integrated workflow

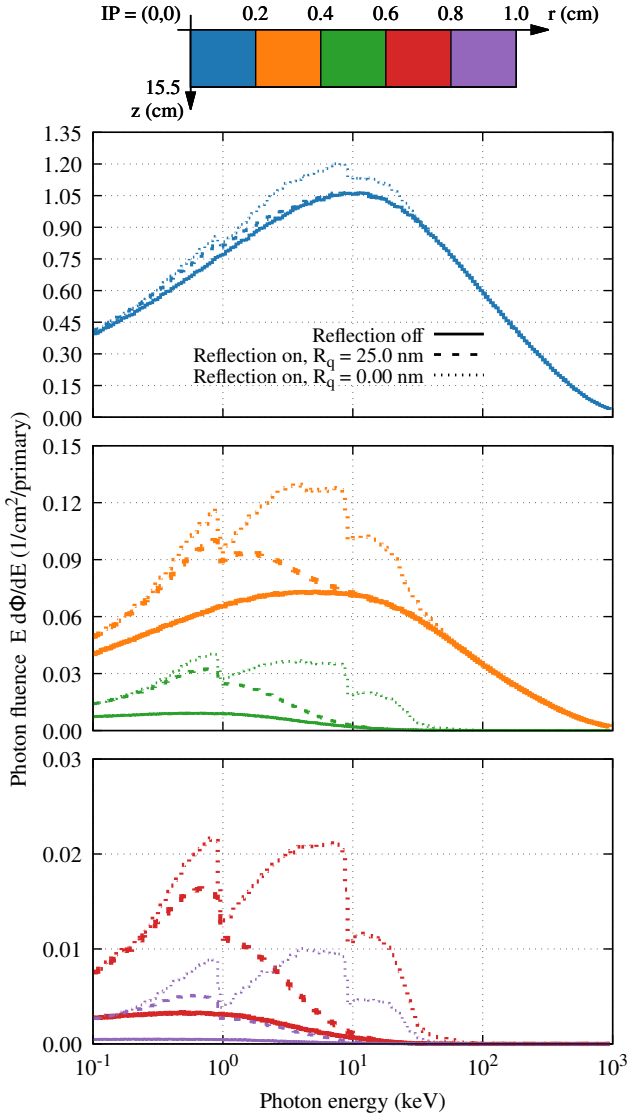


FIG. 17. Energy-differential photon fluence at various radial distances from the IP (see colour code in top diagram and the text for more details), obtained with x-ray reflection deactivated (solid line) and activated on mirror-like surfaces (dotted line) and with a roughness characterised by $R_q = 25$ nm (dashed line).

drastically simplifies the concatenation of tools often required in synchrotron-light beamline studies.

Two applications have been presented, showcasing the performance of this new model. On the one hand, the reflection of synchrotron light on a multilayer mirror in the MINERVA beamline at the ALBA synchrotron has been explained, allowing the radiation study to be handled in a single FLUKA run, instead of the various simulation tools and steps that were previously required. On the other hand, we show how this new FLUKA capability allows one to assess the photon flux throughout the machine and especially around the interaction point of the FCC-ee due to upstream x-ray reflection within the beam pipe. Thus, the model presented here offers enhanced capabilities in the design of accelerator beamline elements. It is included in the public release of FLUKA as of version 4-6.0.

VII. Acknowledgements

This work was done on behalf of the FLUKA.CERN Collaboration. The activity at Argonne National Laboratory was supported by U.S. Department of Energy, Office of Basic Energy Sciences, under contract No. DE-AC02-06CH11357.

[1] A. Devienne and M. García-Fusté, Shielding calculations for the design of new beamlines at ALBA synchrotron, *Radiation Physics and Chemistry* **171**, 108759 (2020).

[2] C. Sunil, Radiation shielding analysis of the concrete hutch of a long beamline of the advanced photon source upgrade project, *Nuclear Instruments and Methods in Physics Research Section A: Accelerators, Spectrometers, Detectors and Associated Equipment* **968**, 163953 (2020).

[3] C. Sunil, Radiation shielding analysis of the small-angle x-ray scattering flight tube end station of aps upgrade project, *Nuclear Instruments and Methods in Physics Research Section B: Beam Interactions with Materials and Atoms* **484**, 48 (2020).

[4] Y. Asano and N. Sasamoto, Development of shielding design code for synchrotron radiation beam line, *Radiation Physics and Chemistry* **44**, 133 (1994).

[5] M. S. del Rio and R. J. Dejus, XOP v2.4: recent developments of the x-ray optics software toolkit, in *Advances in Computational Methods for X-Ray Optics II*, Vol. 8141, International Society for Optics and Photonics (SPIE, 2011) p. 814115.

[6] C. Ahdida, D. Bozzato, D. Calzolari, F. Cerutti, N. Charitonidis, A. Cimmino, A. Coronetti, G. L. D'Allessandro, A. Donadon Servelle, L. S. Esposito, R. Froeschl, R. G. Alia, A. Gerbershagen, S. Gilardoni, D. Horvath, G. Hugo, A. INFntino, V. Kouskoura, A. Lechner, B. Lefebvre, G. Lerner, M. Magistris, A. Manousos, G. Moryc, F. O. Ruiz, F. Pozzi, D. Prelipcean, S. Roesler, R. Rossi, M. S. Gilarte, F. S. Pujol, P. Schoofs, V. Stransky, C. Theis, A. Tsinganis, R. Versaci, V. Vlachoudis, A. Waets, and M. Widorski, New Capabilities of the FLUKA Multi-Purpose Code, *Frontiers in Physics* **9**, 788253 (2022).

[7] G. Battistoni, T. Boehlen, F. Cerutti, P. W. Chin, L. S. Esposito, A. Fassò, A. Ferrari, A. Lechner, A. Empl, A. Mairani, A. Mereghetti, P. Garcia Ortega, J. Ranft, S. Roesler, P. R. Sala, V. Vlachoudis, and G. Smirnov, Overview of the FLUKA code, *Nucl. Instrum. Meth. A* **82**, 10 (2015).

[8] The Official CERN FLUKA website, <https://fluka.cern>, last accessed: January 7, 2026.

[9] G. Hugo *et al.*, Latest FLUKA developments, *Nucl. Instrum. Meth. A* **10**, 20 (2024).

[10] S. Agostinelli, J. Allison, and K. A. *et al.*, Geant4 - a simulation toolkit, *Nucl. Instrum. Meth. A* **506**, 250 (2003).

[11] S. T. *et al.*, Recent improvements of the particle and heavy ion transport code system – PHITS version 3.33, *J. Nucl. Sci. Tech.* **61**, 127 (2024).

[12] F. Salvat, *PENELOPE-2018: A code System for Monte Carlo Simulation of Electron and Photon Transport* (OECD/NEA Data Bank, Issy-les-Moulineaux, France, 2018. Available in PDF format from <http://www.nea.fr/lists/penelope.html>).

[13] M. S. del Rio and L. Rebuffi, Oasys: A software for beam-line simulations and synchrotron virtual experiments, *AIP Conference Proceedings* **2054**, 060081 (2019).

[14] D. L. Windt, Imd—software for modeling the optical properties of multilayer films, *Computer in Physics* **12**, 360 (1998).

[15] R. Assmann, M. Lamont, and S. Myers, A brief history of the LEP collider, *Nuclear Physics B - Proceedings Supplements* **109**, 17 (2002).

[16] G. von Holtey, A. H. Ball, E. Brambilla, H. Burkhardt, P. Estabrooks, F. J. Harris, G. Lutters, J. Rothberg, P. Roudeau, P. Siegrist, J. Wear, P. Weber, and E. Valazzza, Study of beam-induced particle backgrounds at the LEP detectors, *Nucl. Instrum. Meth. A* **403**, 205 (1998).

[17] Future Circular Collider study, <https://fcc.web.cern.ch/>, last accessed: January 7, 2026.

[18] D. Heinis and A. C. *et al.*, MINERVA, a new x-ray facility at the ALBA Synchrotron devoted to assemble and characterize the Silicon Pore Optics Mirror Modules for the NewATHENA mission, in *Space Telescopes and Instrumentation 2024: Ultraviolet to Gamma Ray*, Vol. 13093 (SPIE, 2024) p. 130934X.

[19] Crystal channeling and associated phenomena can however be treated [9].

[20] B. Henke, E. Gullikson, and J. Davis, X-ray interactions: Photoabsorption, scattering, transmission, and reflection at $e=50\text{-}30000$ ev, $z=1\text{-}92$, *Atomic Data and Nuclear Data Tables* **54**, 181 (1993).

[21] S. Caticha-Ellis, Anomalous dispersion of X-rays in crystallography: The contribution of resonance or dispersion effects to the atomic scattering factors, Pamphlet No. 8, International Union of Crystallography (1974).

[22] D. T. Cromer and D. Liberman, Relativistic calculation of anomalous scattering factors for x rays, *The Journal of Chemical Physics* **53**, 1891 (1970).

[23] L. Kissel, B. Zhou, S. C. Roy, S. K. S. Gupta, and R. H. Pratt, The validity of form-factor, modified-form-factor and anomalous-scattering-factor approximations in elastic scattering calculations, *Acta Crystallographica Section A* **51**, 271 (1995).

[24] D. E. Cullen, J. H. Hubbell, and L. D. Kissel, *EPDL97: The Evaluated Photon Data Library, '97 Version*, Tech. Rep. UCRL-50400; Vol. 6; Rev. 5 (Lawrence Livermore National Laboratory, Livermore, CA, USA, 1997).

[25] D. E. Cullen, *EPICS2014: Electron Photon Interaction Cross Sections (Version 2014)*, Tech. Rep. IAEA-NDS-218, Rev. 1 (International Atomic Energy Agency, Vienna, Austria, 2015).

[26] Center for X-Ray Optics, https://henke.lbl.gov/optical_constants/asf.html, last accessed: January 7, 2026.

[27] C. Chantler, K. Olsen, R. Dragoset, A. Kishore, S. Kotchigova, and D. Zucker, X-ray form factor, attenuation, and scattering tables (2003), last accessed: January 7, 2026.

[28] S. L. Adler, Quantum theory of the dielectric constant in real solids, *Phys. Rev.* **126**, 413 (1962).

[29] R. W. James, *The Optical Principles of the Diffraction of X-rays*, The Crystalline State, Vol. 2 (1948).

[30] J. D. Jackson, *Classical Electrodynamics*, 2nd ed. (John Wiley & Sons, Inc., 1975).

[31] A. T. Macrander and X. Huang, Synchrotron x-ray optics, *Annual Review of Materials Research* **47**, 135 (2017).

[32] L. G. Parratt, Surface studies of solids by total reflection of x-rays, *Phys. Rev.* **95**, 359 (1954).

[33] L. Nérot and P. Croce, Caractérisation des surfaces par réflexion rasante de rayons x. application à l'étude du polissage de quelques verres silicates, *Rev. Phys. Appl. (Paris)* **15**, 761 (1980).

[34] S. K. Sinha, E. B. Sirota, S. Garoff, and H. B. Stanley, X-ray and neutron scattering from rough surfaces, *Phys. Rev. B* **38**, 2297 (1988).

[35] ISO 4287: Geometrical product specifications (GPS) — surface texture: Profile method — terms, definitions and surface texture parameters (1997), ISO 4287:1997.

[36] M. L. M. Pont, E. Boter, Magnets for the storage ring alba, in *Proc. EPAC'06* (2006) p. 2562.

[37] A. Frasca *et al.*, Radiation load from radiative Bhabha scattering in the FCC-ee experimental insertions, in *Proc. IPAC'25*, IPAC'25 - 16th International Particle Accelerator Conference No. 16 (JACoW Publishing, Geneva, Switzerland, 2025) pp. 478–481.

[38] K. Oide *et al.*, Design of beam optics for the future circular collider e^+e^- collider rings, *Phys. Rev. Accel. Beams* **19**, 111005 (2016).

[39] K. Oide, Optics with finite chromaticities, presented at 193rd FCC-ee Accelerator Design Meeting, CERN, Meyrin, Switzerland, Oct. 2024.

[40] CERN optics repository, <https://acc-models.web.cern.ch/acc-models/fcc/>, last accessed: January 7, 2026.

[41] K. D. J. André, M. Benedikt, K. Oide, and F. Zimmermann, FCC-ee Collider Design Overview, *PoS ICHEP2024*, 830 (2025).

[42] B. Humann, F. Cerutti, and R. K. et al., Synchrotron Radiation Impact on the FCC-ee Arcs, JACoW **IPAC2022**, 1675 (2022).